JAERI-M
84-011

EVALUATION OF THERMAL STRESS IN
THE ANODE CHAMBER WALL OF A LARGE
VOLUME MAGNETIC BUCKET ION SOURCE

February 1 9 8 4

Russell WELLS,*Hiroshi HORIIKE, Masaaki KURIYAMA
and Yoshihiro OHARA

日 本 原 子 力 研 究 所
Japan Atomic Energy Research Institute

Evaluation of Thermal Stress in the Anode Chamber Wall
of a Large Volume Magnetic Bucket Ion Source

Russell WELLS[*], Hiroshi HORIIKE, Masaaki KURIYAMA and
Yoshihiro OHARA

Department of Thermonuclear Fusion Research,
Tokai Research Establishment, JAERI

Thermal stress analysis was performed on the plasma chamber of the
Large Volume Magnetic Multipole Bucket Ion Source (LVB) designed for use
on the JT-60 NBI system. The energy absorbed by the walls of the plasma
chambers of neutral beam injectors is of the order of 1% of the
accelerator electrical drain power. A previous study indicates that a
moderately high heat flux, of about $600W/cm^2$, is concentrated on the
magnetic field cusp lines during normal full power operation. Abnormal
arc discharges during conditioning of a stainless steel LVB produced
localized melting of the stainless steel at several locations near the
cusps lines. The power contained in abnormal arc discharges (arc spots)
was estimated from the observed melting. Thermal stress analysis was
performed numerically on representative sections of the copper LVB
design for both stable and abnormal arc discharge conditions. Results
show that this chamber should not fail due to thermal fatigue stesses
arising from normal arc discharges. However, fatigue failure may occur
after several hundred to a few thousand arc spots of 30mS duration at
any one location. Limited arc discharge operation of the copper bucket
was performed to partially verify the chamber's durability.

---

* On leave from Lawrence Berkeley Laboratory, Univ. of California

大容積バケット型イオン源ソースチェンバーの熱応力評価

日本原子力研究所東海研究所核融合研究部
R. WELLS＊・堀池　寛・栗山　正明・小原　祥裕

　　ＪＴ－６０用イオン源として設計された大容積バケットソースの熱応力解析について報告する。バケットのチェンバー壁面に入射するパワーはイオンビームパワーの約１％のオーダーで，過去の実験から正常放電中には最大６００Ｗ／cm^{2}の熱流束が磁気カスプライン上に集中してくることがわかっている。またＳＵＳ製バケットソースを使ったイオン源のエージング中にカスプライン近くに局所的な表面のとけた跡が何ケ所も形成され，この事から異常放電（アークスポット）発生時のチェンバー壁面上への熱流束が評価できる。これらの熱入力条件を使用してバケットチェンバーの代表的部分について熱応力解析を行った。計算は材質としては銅を仮定し，正常放電とアークスポットが発生した場合との二通りについて行った。その結果放電が正常な場合には熱疲労による破損の可能性は全く無いことがわかった。一方３０msのアークスポットについては１０００回以上同一の場所で発生すると熱疲労により破損する可能性のあることがわかった。最後にソース部分のみの耐久テストについても簡単に報告する。

＊　派遣研究員；ローレンス・バークレー国立研究所

CONTENTS

目 次

1. INTRODUCTION

The power deposition on the walls of a high current plasma generator is of the order of 1% of the accelerator drain power. Since neutral beam injectors are currently required to operate at quasi-steady state conditions, heat dissipation and thermal stress have become important design factors. Thermal problems are intensified in magnetic multipole bucket designs because the area for particle bombardment is limited to narrow bands at the cusp lines. The JT-60 Large Volume Bucket (LVB) is an extreme example of this geometry. The magnetic field intensity at the inner wall surface is doubled partly through placement of iron strips in channels cut into the outer wall surface beneath the magnets, see Fig.1[1]. Therfore, the width of the particle loss area is much smaller than the previous JT-60 Prototype bucket design. While this geometry has enhanced particle confinement, as evident by the chamber's high arc efficiency and 90% proton ratio, it also has generated concern about the chamber's durability.

To assess the temperature profile within the Large Volume Bucket, the power density distribution over the bucket's walls was experimentally determined[2]. With this data as input, a thermal analysis computer code was used to estimate the temperature distribution in the cusp region. This temperature profile was then input into a stress analysis program to provide an estimate of the thermal stresses.

Operating experience with the LVB indicated that abnormal arc discharges, "arc spots", are not infrequent. These arc spots were found to produce extremely high localized heat loads. Melted regions formed in a stainless steel LVB provided a means of estimating the intensity and size of these discharges. From these estimates thermal stress and fatigue life estimates were made for a small representative section of the bucket wall at the cusp using the coupled thermal and stress analysis programs.

2. OPERATING EXPERIENCE

The following is a summary of relevant operating experience on magnetic multicusp bucket type plasma generators at JAERI.

2.1 JT-60 Prototype Bucket (80% proton ratio).

During operation, this stainless steel bucket acquired a coarsening of the inner surface on narrow strips at the cusp lines. These strips were generally 3 to 5mm wide but many contained multiple shallow melted regions of 4 to 6mm wide by 10 to 50mm long near the filament legs. These melted areas were believed to have been formed by abnormal arc discharges (arc spots) during conditioning at an arc discharge power of up to 60kW[2].

2.2 Stainless steel Large Volume Bucket (90% proton ratio).

The LVB chamber also exhibited a course surface trace on the cusp lines after 2 days of conditioning up to 50 kV, 20A, 0.2s. During filament configuration tests, consisting of 1.5 days of short pulse "arc only" operation, melted regions of 1 to 2mm by 10 to 15mm were formed at 20 locations near the negative filament legs. These regions ran parallel to the cusp trace but were offset by 1 to 1.5mm. During these tests the bucket's operation was frequently unstable leading us to conclude that arc spots and not the normal arc discharge was responsible for the melting.

In view of these results, the chamber wall material was changed to oxygen free copper for future production units of this design[3] because of OFHC's superior thermal properties. Operating experience also suggested a logical division of the thermal stress analysis into stress arising from (1) normal discharge at long pulse durations and (2) "arc spotting".

3. THERMAL STRESS ANALYSIS

3.1 Normal Arc Discharge

3.1.1 Heat Load

During normal operation of the large volume bucket, a moderately high heat flux is concentrated on the cusp lines. Measurements of the cusp heat flux profiles were performed by passing a thermocouple probe across the cusp lines in a perpendicular direction. These measurements did not directly establish quantitative values of the flux intensities but they did confirm that the cusp width is approximately 2 mm and they provided relative intensities. The peak flux at the cusp lines in the central portion of the chamber, near the filaments, was found to be about 2.5 times higher than at cusps near the flanged ends of the chamber and 60 times higher than at off-cusp locations[2]. Infared thermographic imaging of the exterior of the chamber indicated that the flux intensity exhibits a broad profile along the cusp line with maximum temperatures located near the filaments. By combining the probe measurements with the measured total absorbed power and the observed temperature profiles, the most intensely heated cusps were estimated to be subjected to a power density of 600 W/cm^2 [2].

3.1.2 Computer Model

To determine the magnitude of the temperature rise and resultant thermal stress, a finite difference thermal code, HEATING3[4], and a finite element stress analysis program, SAPV[5], were employed. As a first step a small section of the cusp line was modeled (denoted WALL3) as shown in Fig. 2. Unfortunately, the stress intensity proved to be a strong function of the imposed boundary constraints as well as the applied heat load. When the boundary planes perpendicular to the cusp line were fixed, the maximum stress exceeded the yield stress level, but if these planes were allowed to move freely then the stress level was well below yield. These preliminary findings indicated that (1) the

stress level is non-trivial and (2) a more extensive model is needed to accurately simulate the resistance to thermal expansion provided by the wall material surrounding the small section model.

A new larger model, designated WALL6, was developed to more accurately simulate the constraint conditions. WALL6 as shown in Fig. 3a is a model of one quadrant of a full cusp line. Since the central magnetic cusps are spaced 5 cm apart, a model width of 2.5 cm was chosen. The height is the same as the chamber wall thickness of 1.0 cm and the length is 21.0 cm, half the length of the bucket's side wall. Because of limitations in the HEATING3 code, the cooling tube is represented by a rectangular channel. By symmetry the WALL6 model simulates a 5 cm wide by 42 cm long strip of the chamber's side wall. Fig. 4 is an isometric view of the model showing the element divisions and coordinate system. As shown in this figure, x extends outward perpendicular to the chamber surface; y extends along the cusp line; and z lies parallel to the beam axis. This coordinate system is followed throughout the present report.

The assumed heat flux distribution, shown in Fig. 3b is consistent with the observations mentioned previously. A high heat flux is prescribed for the central cusp region, represented by a 1mm wide strip along the z=0 edge, while the remainder of the surface is subjected to a uniform flux of $10W/cm^2$. The high flux region consists of a central 10cm section of 600 W/cm^2 with $450W/cm^2$ regions on either side. The cusp and the high flux region extend from the y=0 edge to 1.5cm from the extreme edge (y=21cm) of the model. The boundary constraints, listed below, were dictated by symmetry and geometric compatability.

   i)   xy plane at z=0 is fixed in the y direction

   ii) xz plane at y=0 is fixed in the z direction

   iii) y $\geq$ 19.5 at x=0 is fixed in the x direction

The first two boundary conditions are obvious from symmetrical considerations while the third is required to eliminate rotation of the end plane of the model. In the actual situation, rotation of the edge of the chamber's side wall (y=21 cm edge of WALL6) is restrained by the adjoining top and bottom walls. Expansion in the y direction is opposed by the chamber's end flanges, however, the most intensely heated cusps are located relatively far from the flanges and thus are not effectively

restrained from expanding along the y axis.

3.1.3 Results of Computer Modeling

Temperature contours of the heated surface (yz plane) and of a cross section (xz plane) of the model at its' hottest point are shown in Fig. 5 and 6 respectively. As shown in these figures, a maximum temperature rise of $103^{\circ}C$ occurs at the center of the $600W/cm^2$ region. Temperatures fall off rapidly in the directions perpendicular to the cusp and at the end of the cusp line. The lowest temperature rise of $24^{\circ}C$ occurs at the cooling channel. A highly distorted three dimensional representation of the temperature profile of the wall surface is shown in Fig. 7. A heat transfer coefficient of $2.0W/cm^2C$ and a water temperature of $0^{\circ}C$ was assumed in all calculations. The maximum thermal stress predicted by SAPV is $12.7kg/mm^2$ and is located near the heated surface at y=11cm. As evident from the stress contours of this plane, shown in Fig. 8, the peak stress is not at the hot surface but instead is located near the iron-copper interface due to the difference in thermal expansion of the two metals. Stress components for the most highly stressed element are given below in kg/mm^2.

$$\sigma_x = 0.16 \qquad \tau_{xy} = 0.05$$
$$\sigma_y = -12.50 \qquad \tau_{yz} = 0.00$$
$$\sigma_z = -4.62 \qquad \tau_{zx} = 0.10$$

Deflection and expansion of the model can be determined from the translation of individual nodes. Given below are the translations of representative nodes on three orthogonal faces of the model.

Since the z=0 face is fixed, the entries of Table 3.1 are
equivalent to the overall expansion in the z direction, which is
approximately 0.01 mm. Similarly, Table 3.2 indicates that the overall
expansion in the y direction is 0.092 mm. The entries in Table 3.3 show
the deflection of the heated surface of the model. According to these
calculations the maximum deflection of 0.02mm occurs on the cusp at the
center of the high flux region. The deformed shape of the mesh is shown
in Fig. 9. Dashed lines represent the model's undeformed shape while
the solid lines correspond to a highly exagerated deformed shape.

3.1.4 Evaluation of Results

The absence of contraint on the overall expansion in the y and z
directions is a good approximation to actual conditions if the deformed
shape of the modeled section maintains continuity with the adjacent wall
sections of the chamber. One requirement for continuity is satisfied if
the overall expansion of the model in the z direction is uniform for any
given depth, i.e. for any given x. The values for z translation in
Table 3.1 show that the maximum difference in expansion for a given x is
only 0.006mm, therefore this criteria is roughly satisfied. Similarly,
expansion in y is very uniform with less than a 0.001mm difference over
the entire y=21cm plane. These results indicate that the chamber will
uniformly expand in height (y direction) and depth (z direction) in the
central region of the chamber.

While expansion in z at a given depth is relatively uniform, a
slight rotation about the y axis of 0.0008 radians occurs at the z=2.5cm
plane. To maintain continuity, rotation of this plane should not be
allowed. Unfortunately this was not easily implemented in the SAPV
formulation of this problem. To obtain an estimate of the error
introduced by this failure, the moment required to eliminate this
rotation can be computed by treating the model as a plate subject to a
bending moment along the z=2.5cm edge. From plate theory the maximum
compressive stress generated in the heated surface of the model is
calculated from the following;

$$\sigma_z = \frac{- E h}{12 \ (\ 1-\nu^2) \ \rho} \qquad\qquad \sigma_y = \nu \ \sigma_z$$

Table 3.1 Z Translation of the WALL6 Model
at Z=2.5 cm, in mm.

			Y (cm)		
X (cm)	0	6	11	16	21
0	0.0131	0.0139	0.0153	0.0133	0.0097
0.1	0.0123	0.0131	0.0145	0.0129	0.0097
0.4	0.0099	0.0106	0.0121	0.0114	0.0097
1.0	0.0052	0.0058	0.0075	0.0084	0.0097

Table 3.2 Y Translation of the WALL6 Model
at Y=21 cm, in mm.

			Z (cm)		
X (cm)	0	0.3	0.6	1.0	2.5
0	0.0919	0.0918	0.0918	0.0918	0.0920
0.1	0.0922	0.0921	0.0919	0.0919	0.0920
0.4	0.0928	0.0924	0.0921	0.0920	0.0920
1.0	0.0918	0.0916	0.0922	0.0920	0.0920

Table 3.3 X Translation of the WALL6 Model
at X=0, in mm.

			Y (cm)		
Z (cm)	0	6	11	16	21
0	−0.0149	−0.0181	−0.0210	−0.0119	0.0
0.3	−0.0134	−0.0166	−0.0191	−0.0103	0.0
0.6	−0.0115	−0.0146	−0.0170	−0.0087	0.0
1.0	−0.0088	−0.0117	−0.0140	−0.0067	0.0
2.5	+0.0022	−0.0005	−0.0028	0.0	0.0

where E is the modulus, ν is Poisson's ratio, ρ is the radius of curvature, and h is the height of the model. The resulting stress components are $\sigma_y = -0.8 kg/mm^2$ and $\sigma_z = -2.2 kg/mm^2$.

Since the stress intensity is determined by the maximum difference in principal stress components, only the y component will have an effect (refer to the stress components given previously). Since this bending stress component is only 6% of the total y component stress, neglecting this contribution will not seriouly affect the results.

The peak stress intensity of $12.7 kg/mm^2$ exceeds the yield strength of $7.7 kg/mm^2$ for OFHC copper at $130^{\circ}C$, which creates two problems. First, cyclic stress in excess of yield may result in fatique and second, the stress predicted by SAPV is not accurate above the elastic limit. However, the concept of elastic strain invariance, which assumes that the strains derived from elastic calculations are the same as would occur during cyclic plastic straining, can be applied to this situation. According to Manson[6] this method agrees well with cyclic plasticity calculations and a modified version of this method has been adopted by the ASME Pressure Vessel Code for Nuclear Pressure Vessels.

Values for the strain components can be calculated from the stress components of section 3.1.3 by use of the elastic stress-strain relations. Ignoring the small shear components, the strain components are;

$$\varepsilon_x = 5.17 \times 10^{-4} \qquad \varepsilon_y = -9.84 \times 10^{-4} \qquad \varepsilon_z = 0.96 \times 10^{-4}$$

Since the material is in a state of tri-axial strain, an equivalent strain range must be computed so that a lifetime estimate can be made from uniaxial test data in the literature. The equivalent strain-range, eq is related to the strain components by the following [6];

$$\Delta\varepsilon_{eq} = \frac{\sqrt{2}}{3} \left[\{\Delta(\varepsilon_x - \varepsilon_y)\}^2 + \{\Delta(\varepsilon_y - \varepsilon_z)\}^2 + \{\Delta(\varepsilon_z - \varepsilon_x)\}^2 \right]$$

Assuming that the strains are fully reversed during cooling, the value of the strain range of component differences is equal to two times the difference, eg. $\Delta(\varepsilon_x - \varepsilon_y) = 2(\varepsilon_x - \varepsilon_y)$. By this method the maximum $\Delta\varepsilon_{eq} = 0.0018$.

Annealed OFHC copper has the property of asymptomically strain hardening during repeated cycling over a fixed strain range. The stress level at which no further hardening occurs is called the "saturation

stress" and is a function of the imposed strain-range. A compilation of the cyclic strain hardening data from Rasmussen and Petersen[7] and Manson[6] for OFHC at room temperature is plotted in Fig. 10. According to this curve the strain-range of 0.18% corresponds to a stress-range of 15kg/mm^2(21.3ksi). Using the SN curve in Fig.11, for life as a function of stress amplitude, the most probable life for 7.5kg/mm^2(10.7ksi), the stress amplitude, is in excess of 10^8 cycles. The extremes of the band on the SN curve represent the 1% and 99% failure limits and thus a cycles to failure range of 3×10^5 to infinite is indicated. Since the highest stresses will ocurr at the highest temperatures, the actual life will be less than that predicted by data from room temperature mechanical strain cycling tests, such as the SN curve of Fig. 10. Additionally, Manson[6] has found that even elevated temperature mechanical cycling tests predict lifetimes up to 2.5 times those found in thermally induced strain cycling at equivalent peak temperatures and strain-ranges. However, in view of the extremely long predicted life and the relatively low peak temperature of the cusp region, these factors are not critical in this case.

3.2 Arc Spots

3.2.1 Heat Flux Estimation

Arc spotting was investigated using the smaller volume, prototype bucket source with the same filaments as the LVB source. It was found that, if no over-current protection was used, multiple spots occur during a single shot, with a duration of 20-50mS and a temporal spacing of 30-100mS between spots[11]. When the protective circuitry was used, the arc was stopped in less than 100mS after a fault condition was detected. Therefore an arc spot duration of approximately 30ms is a reasonable estimate.

To estimate the heat flux required to produce the melted regions, the heat transfer code HEATING3 was used to model a small segment of the stainless steel bucket wall. The model (WALL2) is shown in Figs. 12a and b. The heated region is assumed to be a small rectangular area 10mm x 2mm (5 x 1mm on the model due to symmetry). Melting is assumed to

occur when the temperature rise of the surface exceeds $1400^{\circ}C$, the melting point of stainless steel.

For short heating times, the surface of even a thin conductor may be approximated by a semi-infinite solid. Assuming constant properties, the solution for the temperature, T, at a given depth, x, in a semi-infinite slab is:

$$T - Ti = \frac{2q}{kA} \left[\left(\frac{\alpha\tau}{\pi}\right)^{\frac{1}{2}} \exp\frac{-x^2}{4\alpha\tau} - \frac{x}{2}\left(1 - erf\frac{x}{2\sqrt{\alpha\tau}}\right) \right]$$

with the boundary conditions $T(x,0)=Ti$ and $q/A=-k\ \partial T/\partial x$ for $\tau>0$. Where q/A is the heat flux, k is the conductivity, τ is the heating time, and α is thermal diffusivity[10].

For stainless steel k=16.3 W/mC and $\alpha=4.44\times10^{-5}m^2/s$. The fraction of the temperature rise at a depth of 0.8mm, which is the depth of the stainless steel/iron interface, is indicative of the accuracy of this approximation. For τ=30mS this fraction equals 0.068 and thus only a small amount of the surface temperature rise is present at the stainless steel/iron boundary. Repeating this calculation for τ=50mS gives a fractional rise of 14%. Therefore, the semi-infinite slab is adequate for estimating the surface temperatures of the stainless steel bucket for heating times of less than 50mS.

Fig. 13 shows the heat flux required to produce melting as a function of arc spot duration. For heating times of less than 50mS the analytical solution was used and for times between 50 and 200mS the HEATING3 code was used. The lowest heat flux, $3kW/cm^2$, corresponds to an assumed arc duration of 200mS and the highest flux calculated, $6.8kW/cm^2$, corresponds to a 20mS arc spot. The thermal response of the copper bucket to this range of arc spot duration and intensity combinations was calculated using HEATING3 and the WALL3 model. The resultant surface temperature rise as a function of spot duration is shown in Fig. 14. Note that the temperature rise is approximately constant and well below the melting point due to the higher conductivity of OFHC copper.

3.2.2 Elastic Thermal Stress Calculations

To evaluate the bucket wall's ability to withstand arc spots of 30ms and q/A=5.5kW/cm^2, HEATING3/SAP5 computations were performed on a modified WALL3 model (designated WALL3B). This model has the same features as the original WALL3 model except it has been lengthened in the y-direction to 2.0cm and the mesh spacing in the y-direction has been altered (Fig. 15). The 5.5kW/cm^2 heat flux is imposed over a 5mm X 1mm area on the yz surface along the planes of symmetry and thus represents a 10mm X 2mm spot. All other regions are unheated. As in all previous models, convective cooling is assumed in the water channel with h=2.0W/cm^{2}C and an ambient water temperature of 0°C. The boundaries are fully constrained from expansion in both the y and z directions.

The 2 cm length of this model was chosen to assure that the heated region will be completely enclosed by cool regions at the boundaries. Calculated temperature contours for the various planes are given in Figs. 16a-b with a bird's eye (isometric) view of the surface temperature rise provided in Fig. 17. Note that the temperature rise, having a maximum of 225°C, is confined to the heated corner region. Stress contours of each plane are given in Figs. 18a-c in units of N/cm^2. As evident from these contours, the maximum stress intensity occurs in the surface of the heated corner region, with a value of 32.8kg/mm^2 (32.1X10 N/cm^2).

Mesh spacing can affect the accuracy of both stress and temperature calculations. Since Fig. 16 indicate that a high thermal gradient is present in the heated corner region, a new model was constructed (WALL5) with a finer mesh in this region. The new mesh, shown in Fig. 19 eliminates the complicated geometry at the water channel since WALL3B results indicate that this region has little affect on either the stress or temperature distributions. With the exception of the simplified geometry and finer mesh, this model is the same as WALL3B.

The peak temperature for the WALL5 model is 234°C, which is only slightly greater than prevously predicted, and the temperature distribution, Fig. 20, is nearly identical to the WALL3B case. Stress computations were performed on the WALL5 model for two different boundary conditions. First the model was allowed free expansion in the y and z directions with only the planes of symmetry fixed and second, expansion in y and z was completely constrained. The resulting maximum

stress intensities and stress components for the WALL3B and two WALL5 runs are tabulated below.

Table 3.4   Comparison of the Calculated Stress Values
for the Region of Maximum Stress Intensity
(kg/mm^2)

Component	WALL3B	WALL5	
		no expansion	free expansion
σ_x	$-$ 1.0	$-$ 0.5	$-$ 0.5
σ_y	$-$ 33.9	$-$ 37.2	$-$ 37.0
σ_z	$-$ 14.6	$-$ 14.3	$-$ 14.8
$\tau_{xy}, \tau_{yz}, \tau_{zx}$	0.15	0.1	0.1
$\sigma_{intensity}$	32.8	36.8	36.5

The relatively close agreement between the WALL3B and WALL5 results indicate that the mesh is sufficiently fine for this application. These results also show that the stress state in the region of maximum stress intensity is insensitive to the different applied boundary conditions.

3.2.3   Evaluation of Results

Since the thermal stress level greatly exceeds the yield strength of OFHC copper and in view of the repetitive nature of arc spots, fatique failure of the bucket wall becomes a distinct possiblity. As previously applied to the normal discharge case (section 3.1.4), the method of elastic strain invariance can be used to calculate the equivalent strain-range. Assuming the strain is fully reversed upon cooling the equivalent total strain-range is 0.547%. In addition to arcing, thermal strains are induced during normal arc discharge thus, in the worst case, the strain will be the sum of these two effects. The cumulative strain-range is 0.727%, which corresponds to a room temperature fatigue life of about 8×10^4 with a 1 to 99% failure range of

10^3 to 8×10^4 cycles. However, due to the degradation of copper's mechanical properties with increasing temperature, the actual fatigue life will be less.

Since the spot duration is much shorter than the thermal time response of the bucket wall, the surface temperature rise due to arc spots will be nearly additive to the wall temperature prior to the spot. Therefore, the bucket wall surface may locally reach temperatures of $340^\circ C$ or more if the spot occurs after several seconds of normal discharge. To provide some estimate for life in the present elevated temperature situation the Coffin-Manson fatigue law was used;

$$\Delta \varepsilon_p = C \; N^{\frac{1}{2}} \qquad \text{where} \quad \Delta \varepsilon_p = \text{plastic strain-range}$$

$$N = \text{cycles to failure}$$

$$\text{and} \qquad C = -1/2 \; \ln \left[\frac{100 - RA}{100} \right] \text{ after Osgood[8)}$$

With this empirical relation, the plastic strain-range is computed by subtracting the elastic component from the total strain-range. The elastic strain-range component is assigned the value of $2S/E$ where S is either S_y, the yield strength or S_e, the endurance limit. Life predictions by this method are listed in Table 3.5 for three conditions, (1) arc and normal discharge strain summed but room temperature material properties used, (2) arc spot strain and temperature rise only and (3) normal and arc discharge strain and temperature summed.

Table 3.5 Fatigue Life Estimations from
the Coffin-Manson Fatique Law

Condition	Temp.	$\Delta \varepsilon_{eq}$	$\Delta \varepsilon_p$	C	N
1	R.T.	0.727%	0.592%	0.805	18500
2	$240^\circ C$	0.547%	0.434%	0.200	2100
3	$340^\circ C$	0.747%	0.644%	0.281	1900

The reduction in life with increasing temperature is due to the sharp drop in ductility (RA) in the 170 to $250^\circ C$ range, Fig. 21, and the steady decrease in yield strength from room temperature, Fig. 22.

Condition 1, which is equivalent to the conditions assumed when estimating lifetimes from the SN curve of Fig. 11, shows a rough agreement between the two methods.

The results tabulated in Table 3.5 indicate a fatigue life on the order of 2000 cycles for repetitive arcing at any one location on the bucket wall. As mentioned previously, there is a discrepancy of up to 2.5 times between thermally induced strain and mechanically induced strain at elevated temperatures. Therefore, the best estimate of fatigue life under arc spotting conditions is between 750 and 1900 cycles.

While we have attempted to be conservative in our analysis the premise that the heat flux during arc spots is the minimum required to locally melt the stainless steel bucket is not conservative. Unfortunately this is our only indicator of the flux intensity, so there is an inherent uncertainty in the preceding analysis.

4. LARGE VOLUME BUCKET TESTING

Testing. As mentioned previously, under normal conditions (ie. no arcing) the cusp regions are expected to absorb up to 600 W/cm^2 for 10 seconds. This value was based upon an arc discharge power of 57 kW which is equivalent to 40 A of extracted beam at an arc efficiency of 0.7A/kW. To test the large volume copper bucket design, the source was mounted on the JT-60 NBI Prototype and subjected to over 2400 "arc only" shots. A summary of these tests is provided in Fig. 23. A shot duration of $\geq$ 5 seconds was selected on the basis of the thermal response time of the bucket wall. HEATING3 calculations of the WALL3 model show that the wall surface approaches equilibrium in 5 seconds. Temperature/time histories are shown for selected locations in Fig.24. As shown in Fig. 23, the nominal design power condition was not achieved, however, more than 1300 shots were performed at power levels of 46-51 kW. During these tests many arc spots occured resulting in the destruction of 5 filaments. No air or water leaks were detected during testing and post-test inspection revealed no damage to the bucket wall's inner surface.

Condition 1, which is equivalent to the conditions assumed when estimating lifetimes from the SN curve of Fig. 11, shows a rough agreement between the two methods.

The results tabulated in Table 3.5 indicate a fatigue life on the order of 2000 cycles for repetitive arcing at any one location on the bucket wall. As mentioned previously, there is a discrepancy of up to 2.5 times between thermally induced strain and mechanically induced strain at elevated temperatures. Therefore, the best estimate of fatigue life under arc spotting conditions is between 750 and 1900 cycles.

While we have attempted to be conservative in our analysis the premise that the heat flux during arc spots is the minimum required to locally melt the stainless steel bucket is not conservative. Unfortunately this is our only indicator of the flux intensity, so there is an inherent uncertainty in the preceding analysis.

4. LARGE VOLUME BUCKET TESTING

Testing. As mentioned previously, under normal conditions (ie. no arcing) the cusp regions are expected to absorb up to 600 W/cm^2 for 10 seconds. This value was based upon an arc discharge power of 57 kW which is equivalent to 40 A of extracted beam at an arc efficiency of 0.7A/kW. To test the large volume copper bucket design, the source was mounted on the JT-60 NBI Prototype and subjected to over 2400 "arc only" shots. A summary of these tests is provided in Fig. 23. A shot duration of $\geq$ 5 seconds was selected on the basis of the thermal response time of the bucket wall. HEATING3 calculations of the WALL3 model show that the wall surface approaches equilibrium in 5 seconds. Temperature/time histories are shown for selected locations in Fig.24. As shown in Fig. 23, the nominal design power condition was not achieved, however, more than 1300 shots were performed at power levels of 46-51 kW. During these tests many arc spots occured resulting in the destruction of 5 filaments. No air or water leaks were detected during testing and post-test inspection revealed no damage to the bucket wall's inner surface.

5. CONCLUSIONS

The results of the thermal stress calculations for both normal and arc spot discharge conditions are the product of several assumptions and approximations. For the normal arc discharge case, the heat loads were determined from very limited data at relatively low power conditions and then assumed to scale linearly with arc power. More importantly, the heat flux at only a few cusp locations was amenable to measurement thus requiring the overall distribution to be assumed on the basis of symmetry and educated guess-work. However, the lifetime predicted for normal arc discharge conditions exceeds the requirements by a wide margin, and in view of the conservatism used in this analysis, thermal stress arising from normal arc discharge should not result in damage to the copper source chamber.

Due to the extremely high heat flux contained in arc spots, thermal strains generated by these events are too large to be tolerated for more than a few hundred occurances. The estimated heat flux intensity corresponds to a minimum value, thus the life prediction made in this analysis may be overly optimistic. The limited testing of the bucket during "arc only" operation does provide some evidence that some arc spots can be tolerated without causing melting or other observable damage. However, to insure long term operation of this chamber, the source must be protected from the occurance of frequent arc spots. Thus high speed arc spot detection and switching circuitry has now been installed to both protect the hot filaments and to prolong the chamber life.

ACKNOWLEDGEMENT

The authors are indebted to Drs. M. Akiba and M. Araki for facilitating our use of the JAERI computer system and computer codes. We would also like to thank Drs. S. Tanaka and Y. Okumura for many enlightening discussions and Dr. Matsuda for reviewing the manuscript. Additionally, we would like to acknowledge Drs. M. Tanaka, Y. Obata and Y. Iso for their support and encourgement.

REFERENCES

1) Y. Okumura, H. Horiike, K. Mizuhashi, Rev. Sci. Instrum. 54(12) (1983)

2) H. Horiike, to be sumitted for publication

3) M. Akiba, "Beam Extraction at the Prototype Injector Unit for JT-60", Proc. of the 10th Sympo. on Engineering Problems in Fusion Research, Philadelphia, Pennsylvannia, Dec. 1983

4) W.D. Turner and M. Simon, "HEATING-3 – An IBM 360 Heat Conduction Program", ORNL-TM 3208

5) SAP-V.2, "A Structural Analysis Program for Static and Dynamic Response of Linear Systems", Univ. of So. Cal. (1972)

6) S.S. Manson, Thermal Stress and Low Cycle Fatigue, McGraw-hill, N.Y. (1966)

7) K. Rasmussen and O. Pederson, Acta Met. 28, 1467 (1980)

8) C.C. Osgood, Fatigue Design 2nd ed., Pergamon Press, Toronto (1982)

9) ASM, Metals Handbook, 9th ed., 1, 278

10) J. Holman, Heat Transfer 4th ed. McGraw-Hill, N.Y. (1976)

11) S. Tanaka and Y. Okumura, private communication based on observations of arc spotting with TV cameras.
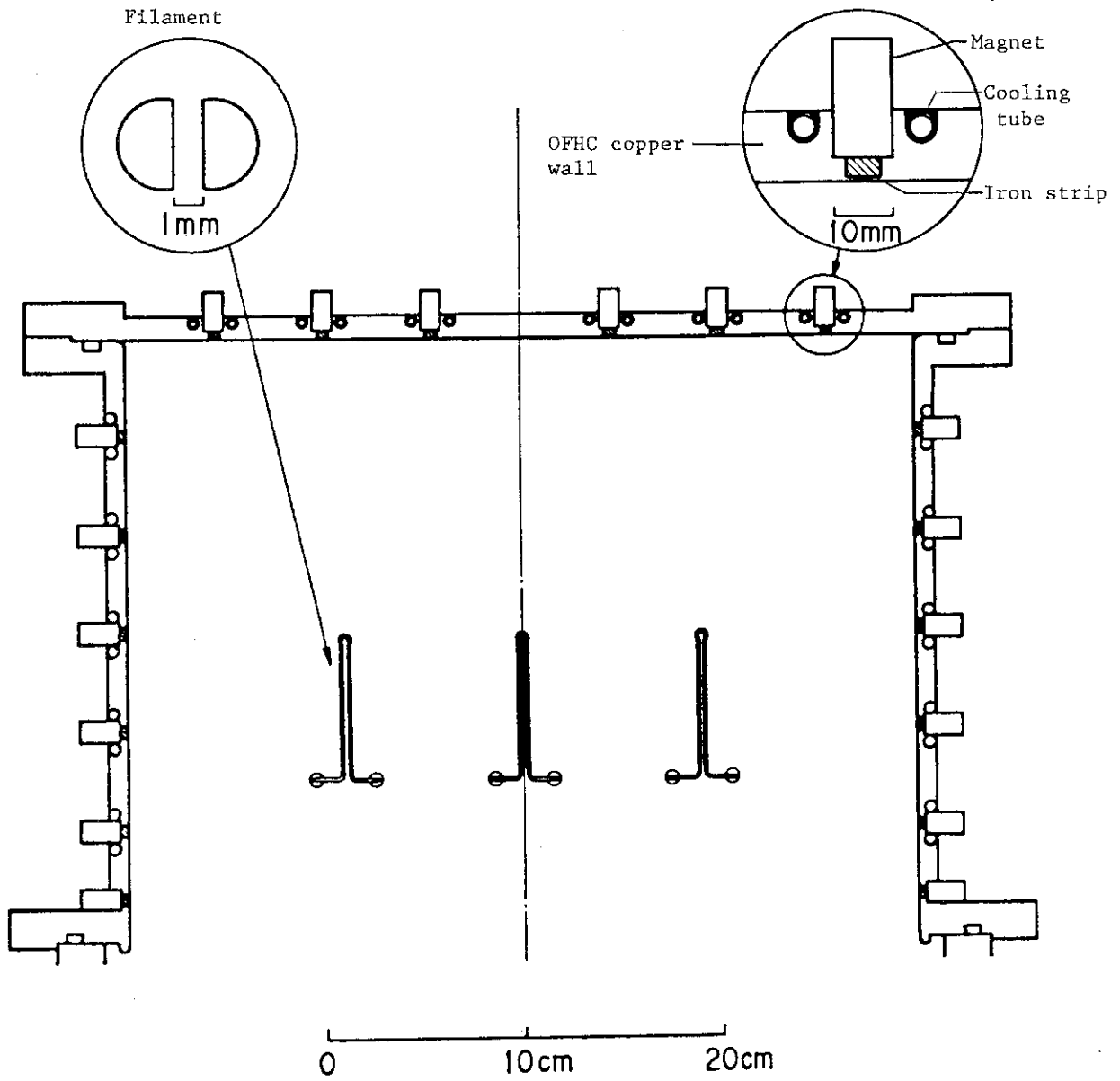
Fig. 1 Cross sectional view of Large-volume, magnetic multipole, plasma chamber.
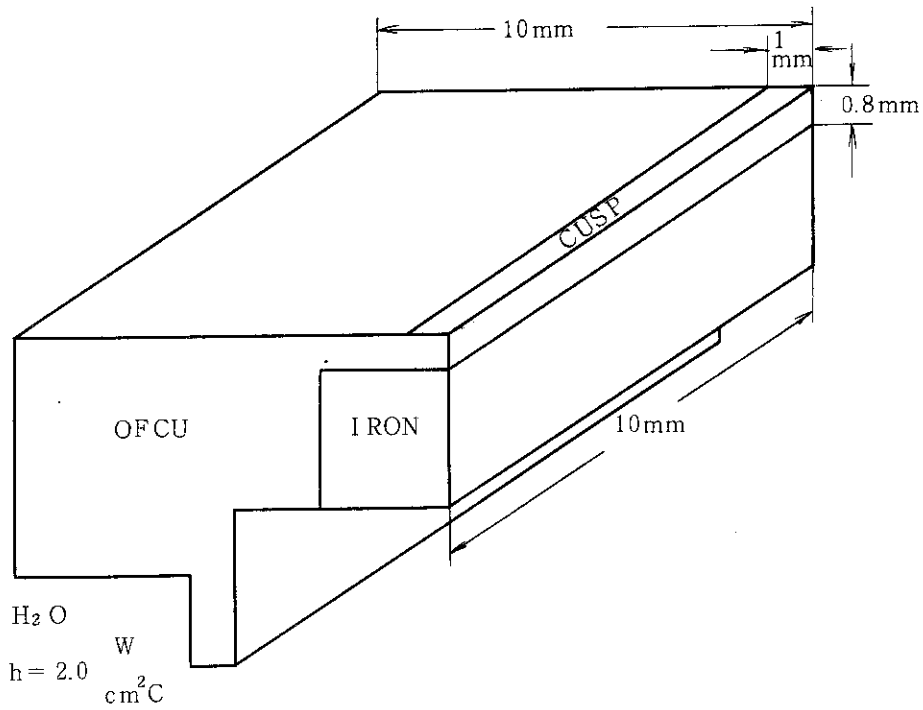
Fig. 2   Isometric drawing of small section, WALL 3, model of copper bucket
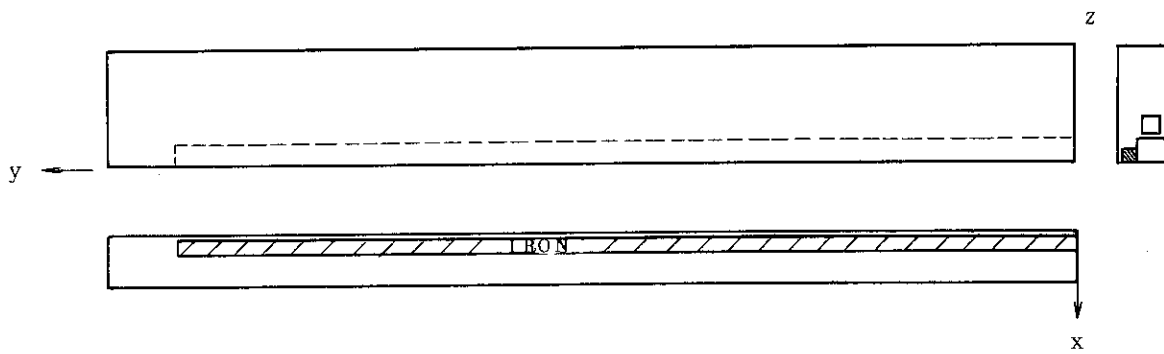
Fig. 3a   Full cusp model, (WALL 6)
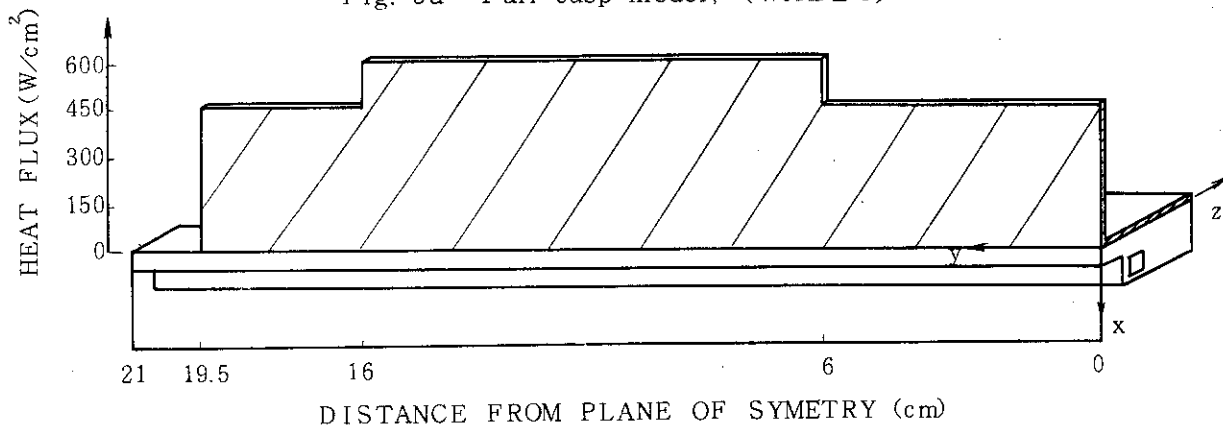
Fig. 3b   Heat flux profile for full cusp model (WALL 6)

WALL6 90% H+ BUCKET – FULL SECTION CUSP MODEL 10/20/83

WATER CHANNEL

X

NOT TO SCALE

IRON

0.4

Z

1.0cm

21.0

2.5

Y
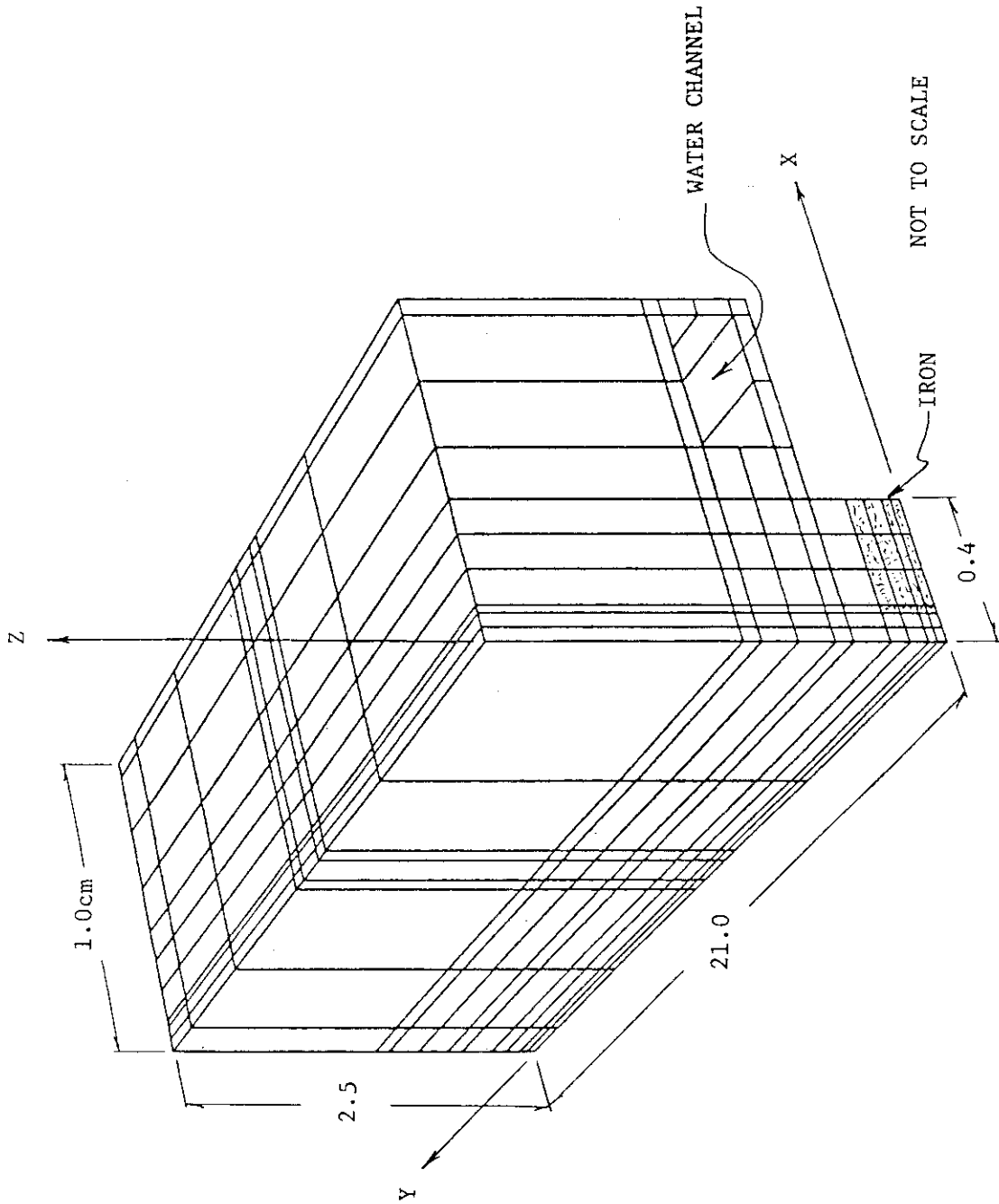
Fig. 4 Isometric view of WALL6 model with element divisions shown

CONTOUR VALUES 10**-1

1	345.6
2	381.9
3	418.3
4	454.6
5	490.9
6	527.3
7	563.6
8	600.0
9	636.3
10	672.6
11	709.0
12	745.3
13	781.6
14	818.0
15	854.3
16	890.7
17	927.0
18	963.3
19	999.7
20	1036.0
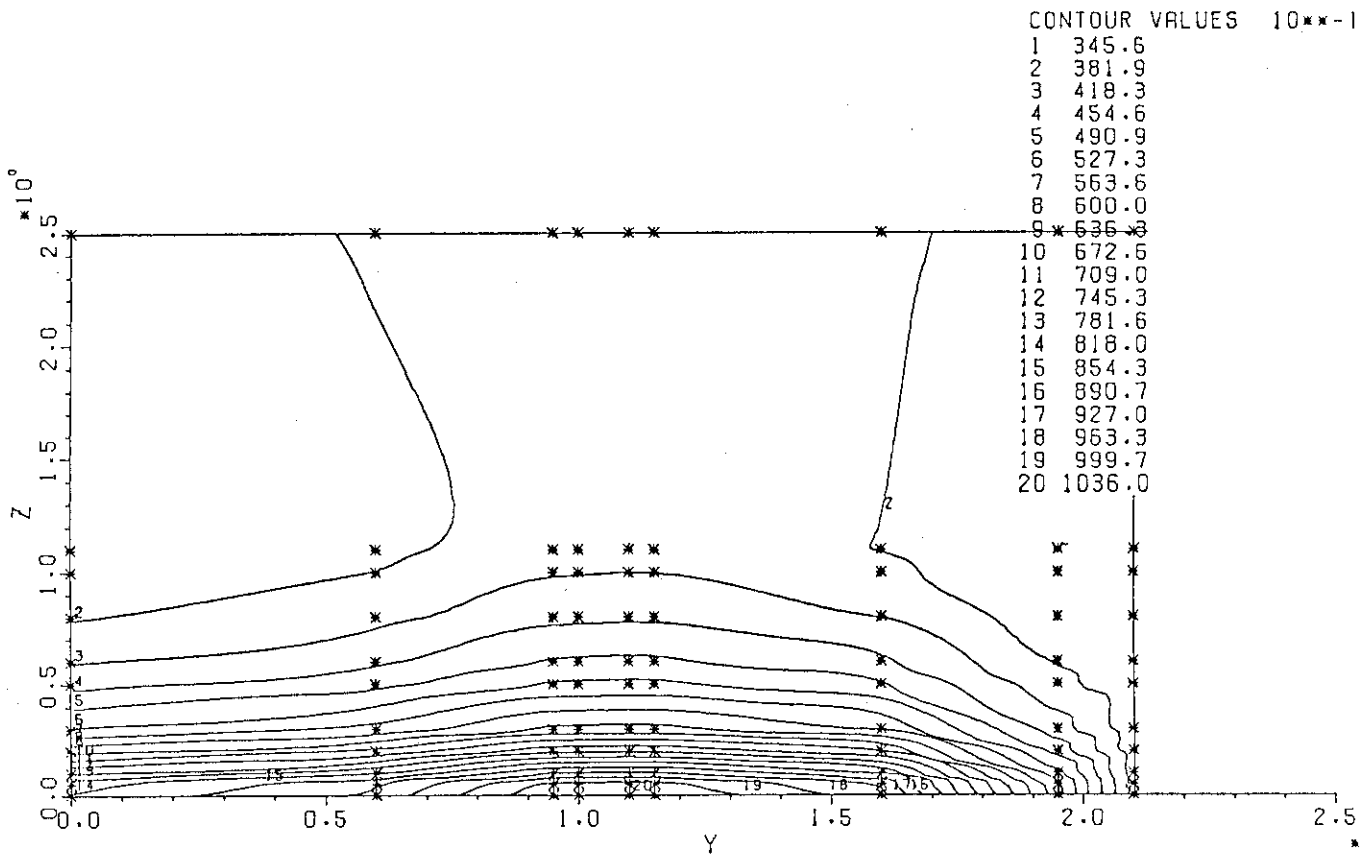
Fig.5　Temperature contours of the WALL6 model's YZ plane at X=0

Y = 1.100E+01

CONTOUR VALUES 10**-1

1	282.9
2	322.5
3	362.2
4	401.8
5	441.4
6	481.1
7	520.7
8	560.4
9	600.0
10	639.6
11	679.3
12	718.9
13	758.5
14	798.2
15	837.8
16	877.5
17	917.1
18	956.7
19	996.4
20	1036.0

H_2O
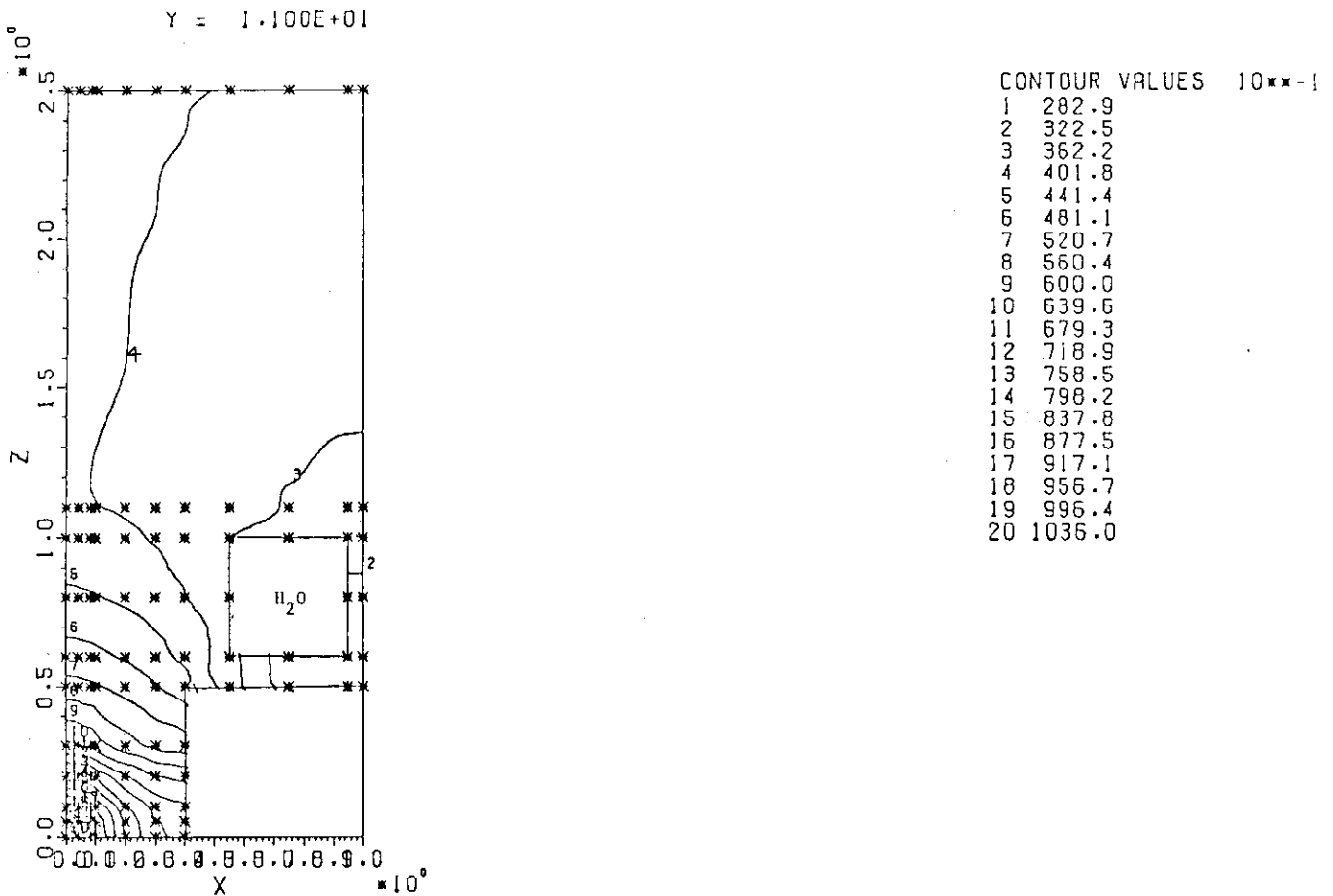
Fig. 6　Temperature contours on the mid-model cross section, XZ plane at Y=11 cm., of the WALL6 model.
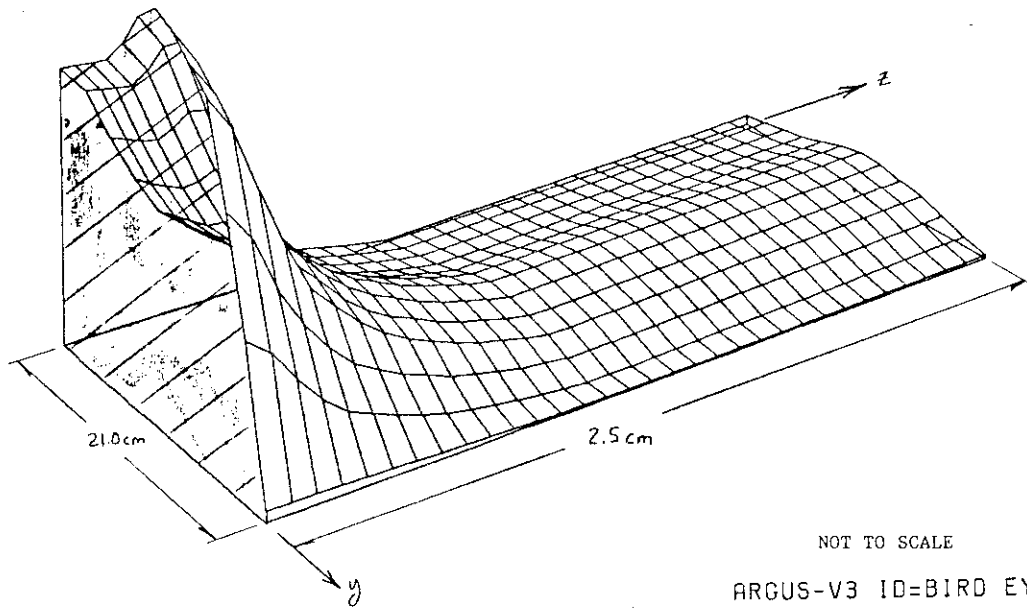
Fig. 7 Three dimensional view of surface temperature of WALL6 model.

CONTOUR VALUES 10** 2 N/cm²

1	2.4
2	8.8
3	15.2
4	21.6
5	28.0
6	34.4
7	40.8
8	47.3
9	53.7
10	60.1
11	66.5
12	72.9
13	79.3
14	85.7
15	92.1
16	98.6
17	105.0
18	111.4
19	117.8
20	124.2
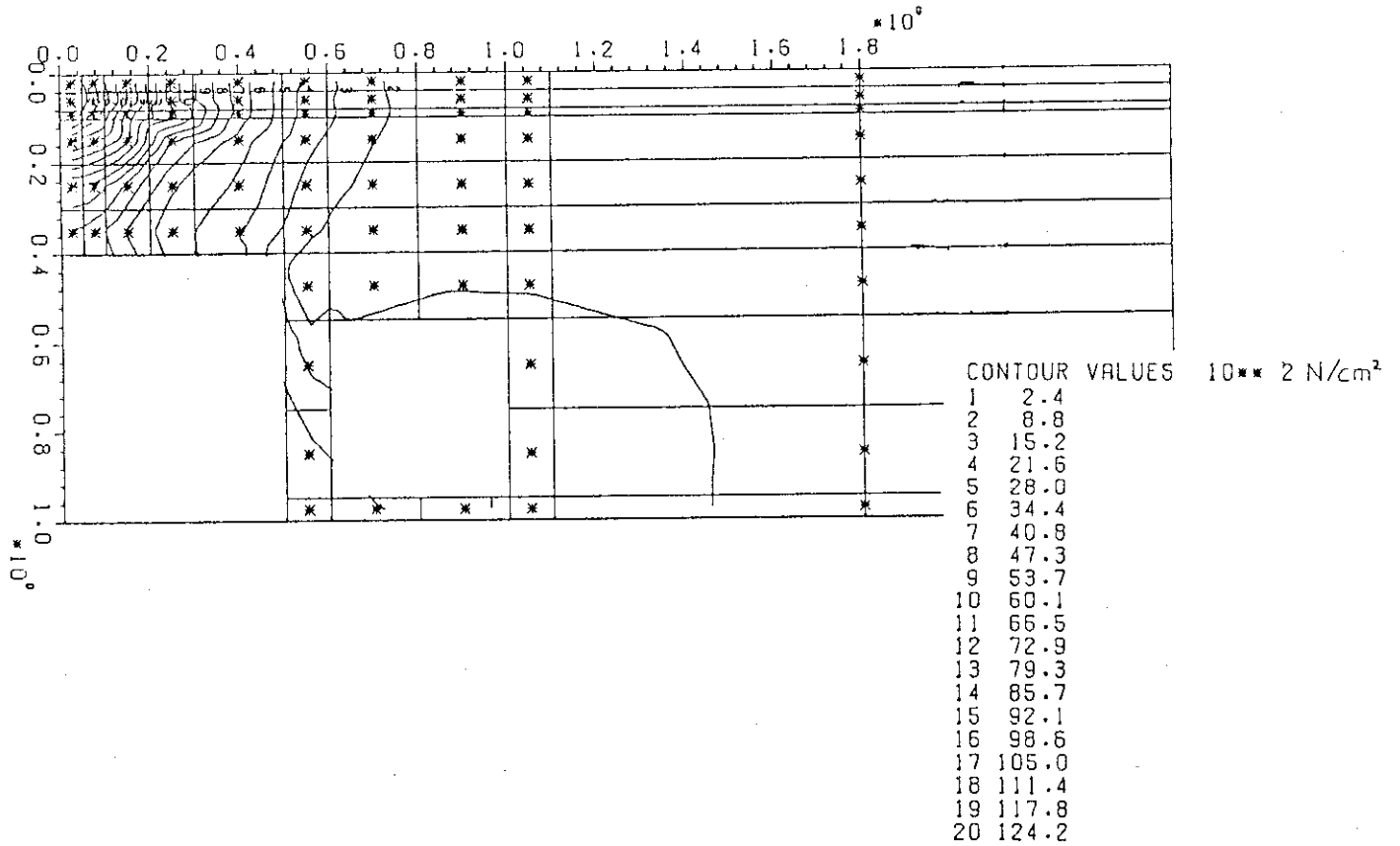
Fig. 8 Stress intensity contours of cross section of Wall6 model at mid-model (XZ plane at Y=11cm.).
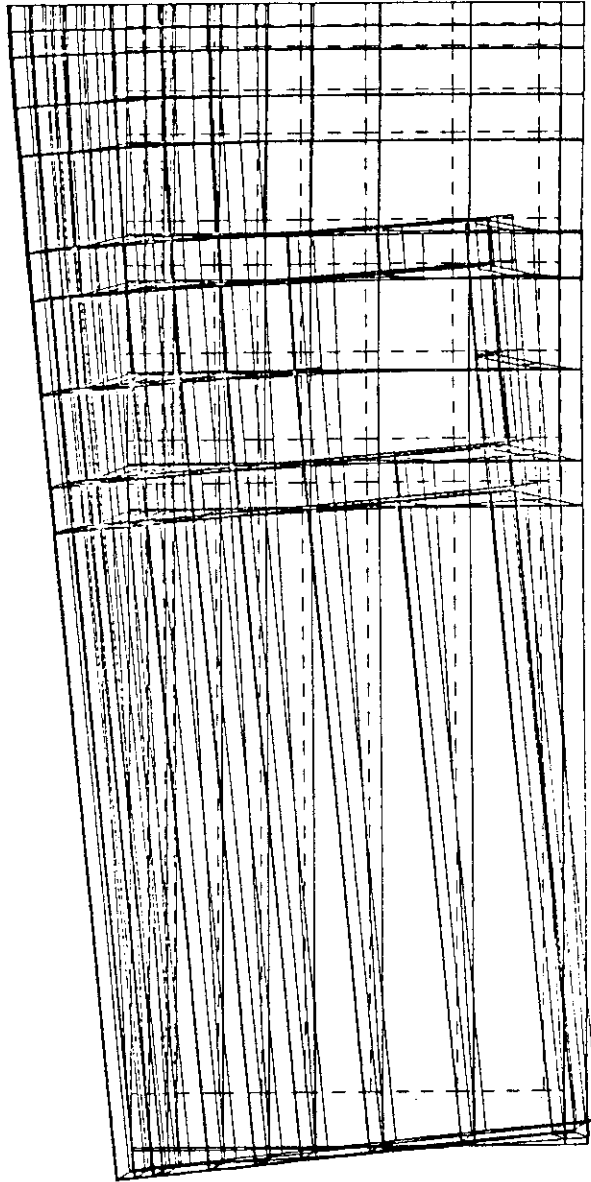
Fig. 9 Deflection of WALL6 model, solid lines represent the deformed shape and dashed lines are the undeformed shape.
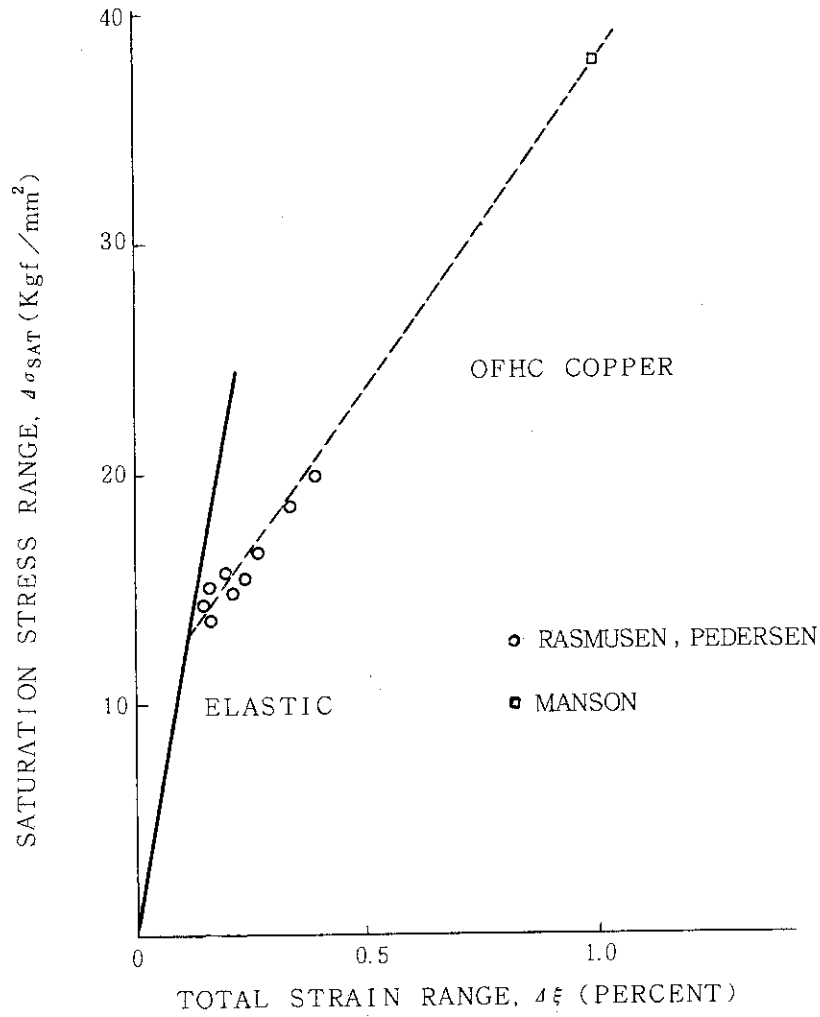
Fig. 10   Strain hardening by cycling at constant
strain-ranges
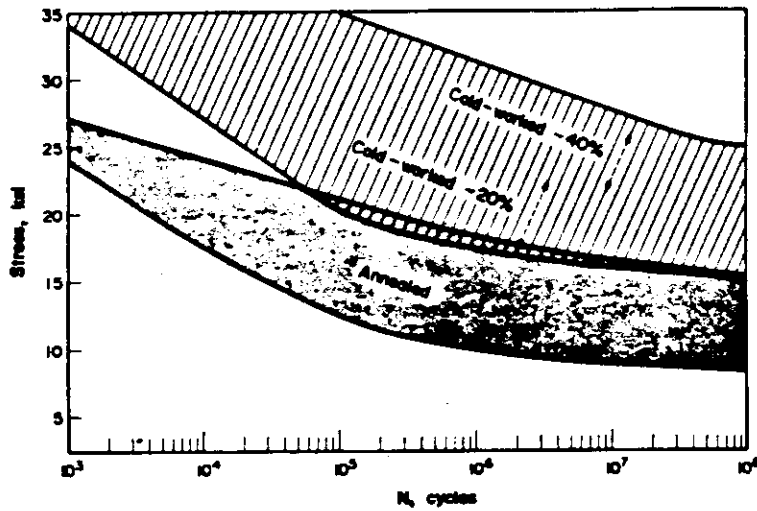
Fig. 11   S-N bands for copper alloy CDA-102 ("OFHC").
R = -1.0, Kt = 1.0.   Room Temperature.
From reference 8.
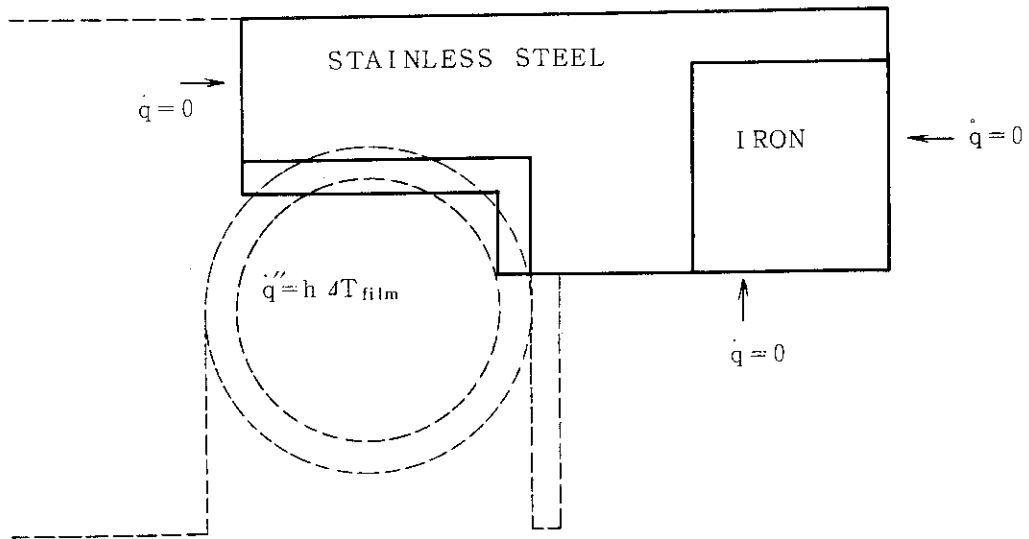
Fig. 12a   Side view of SUS. bucket model outline of bucket
wall cross section in shown as dashed lines
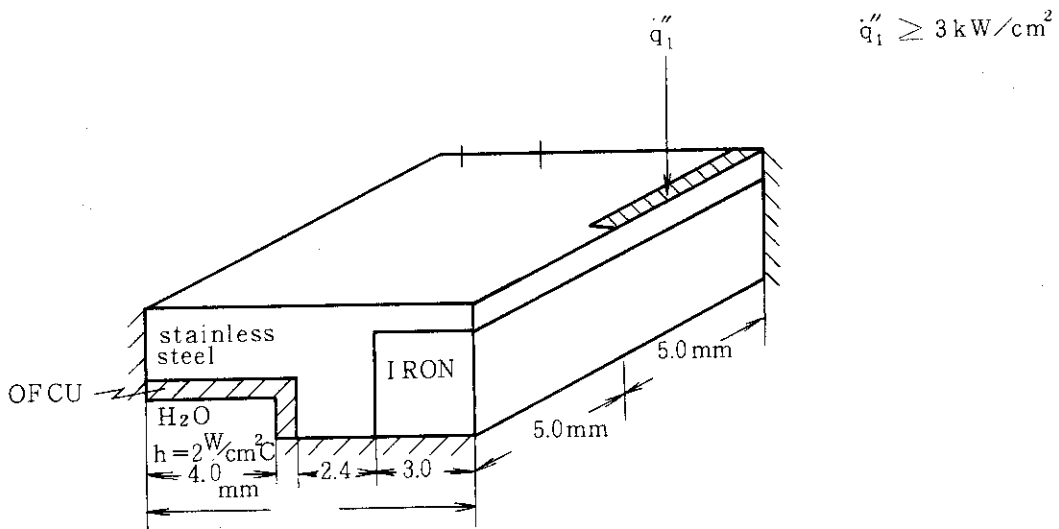
Fig. 12b   Isometric view of SUS. bucket model (WALL 2)
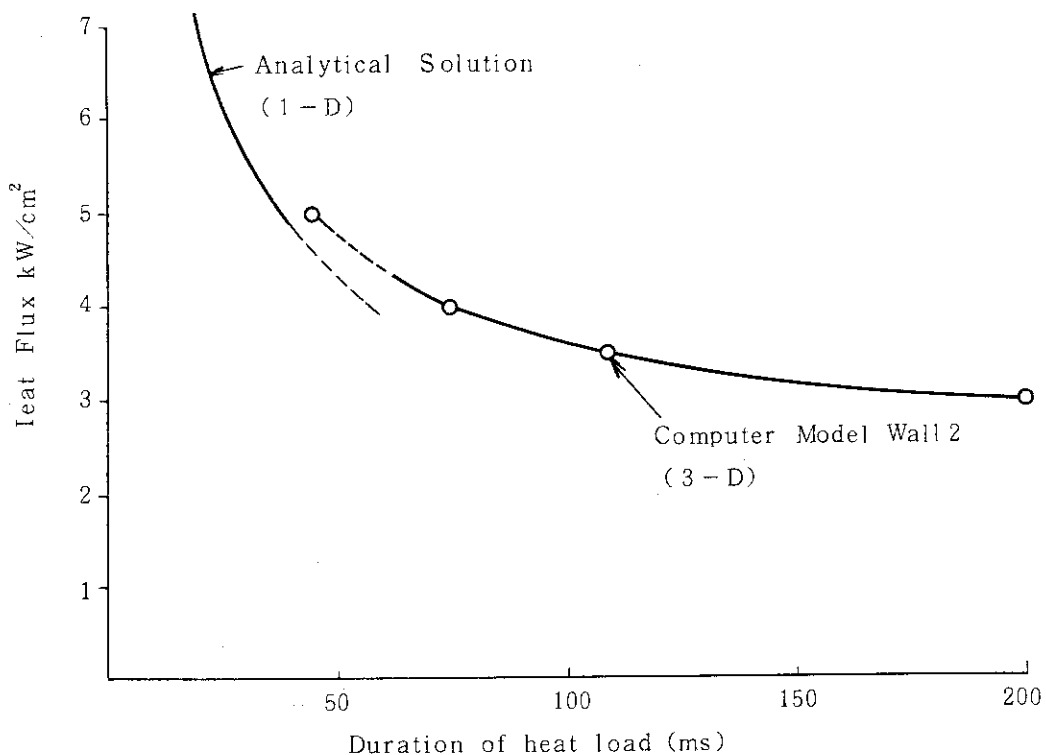
Fig. 13   Heating time required to melt (REACH 1400°C) the
surface of the stainless steel large volume bucket
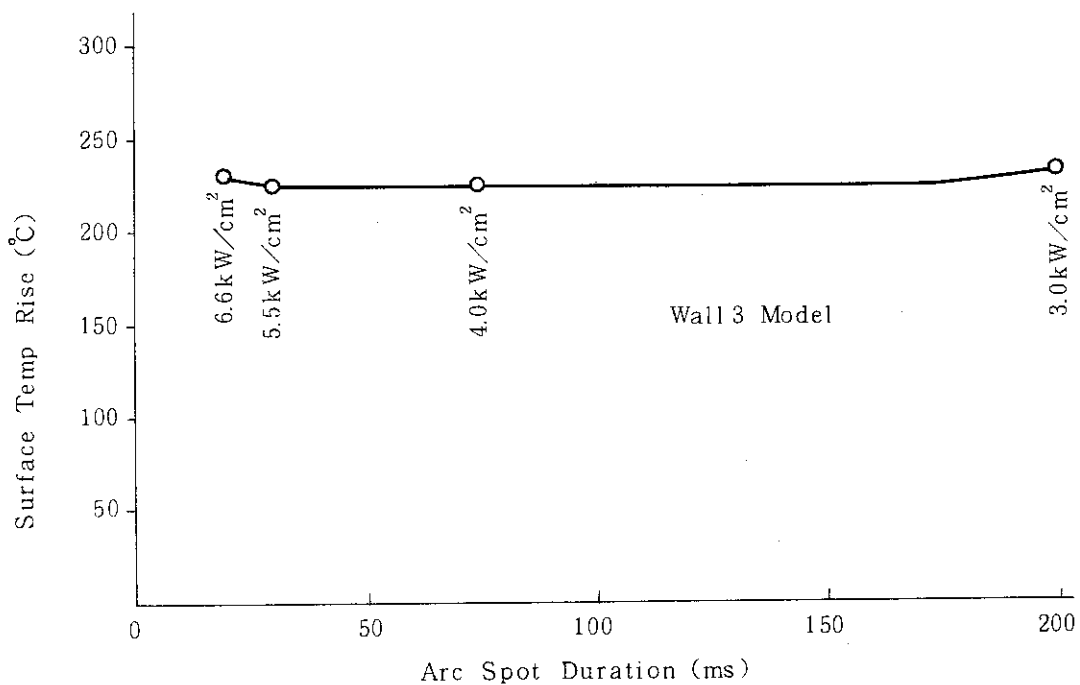
Fig. 14   Surface temp. rise of the copper, large volume bucket,
for combinations of arc spot time and intensity given in
Fig. 13

* SOURCE BUCKET WALL3B 90% H+ COPPER, TRANSIENT

Z

Y

COOLED
SURFACE

10mm

5mm

5.5 KW/cm²

OFHC COPPER

5mm

IRON

X

4mm
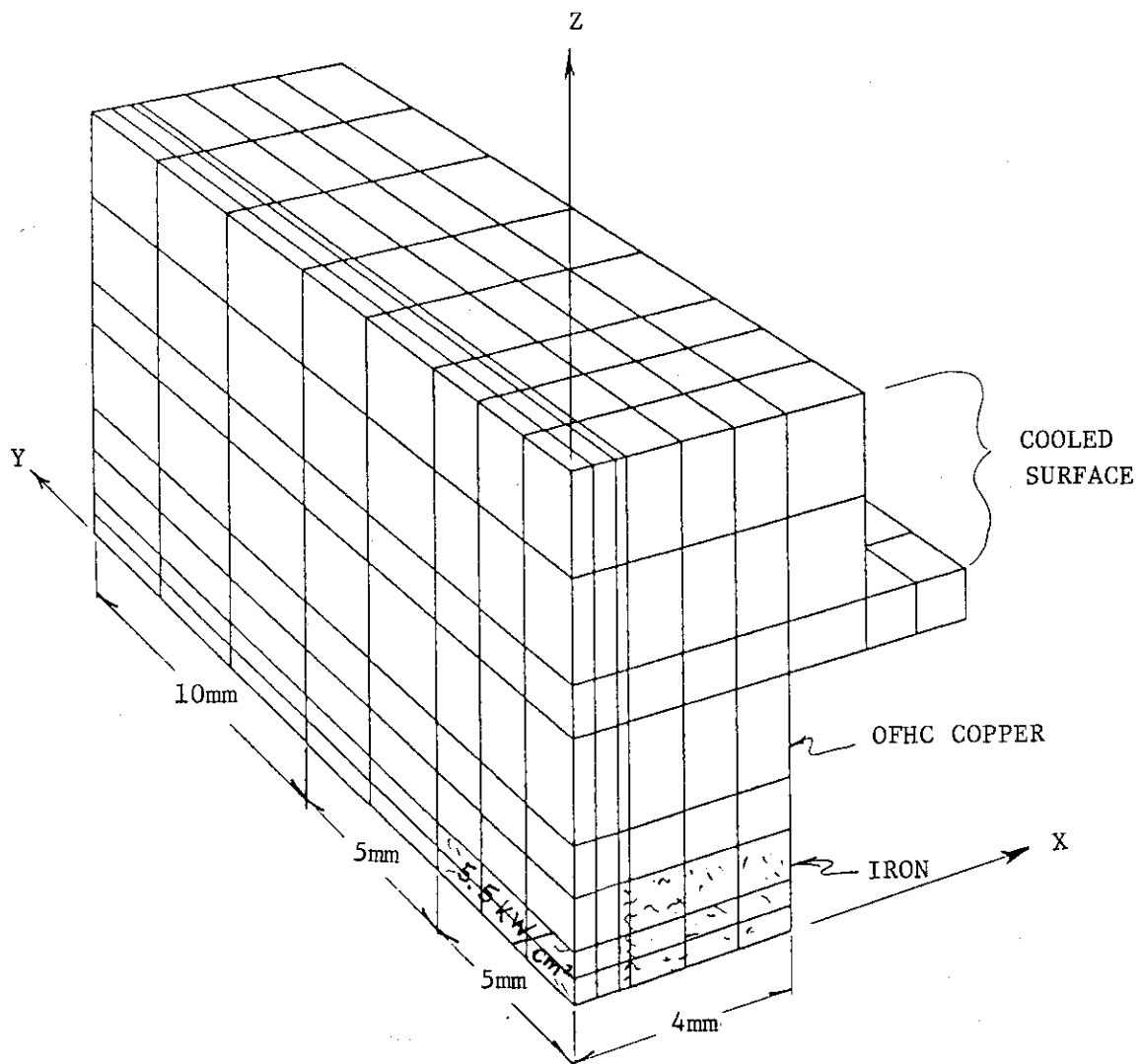
Fig. 15   Three dimensional view of WALL3B mesh.

Fig. 16a Temperature contours on the heated surface of the WALL3R model.

Fig. 16b Temperature contours of the cross section of the WALL3B model at the heated corner.

* SOURCE BUCKET WALL3B 90% H+ COPPER. TRANSIENT 30 C H2O 8/11/83

X = 0.0
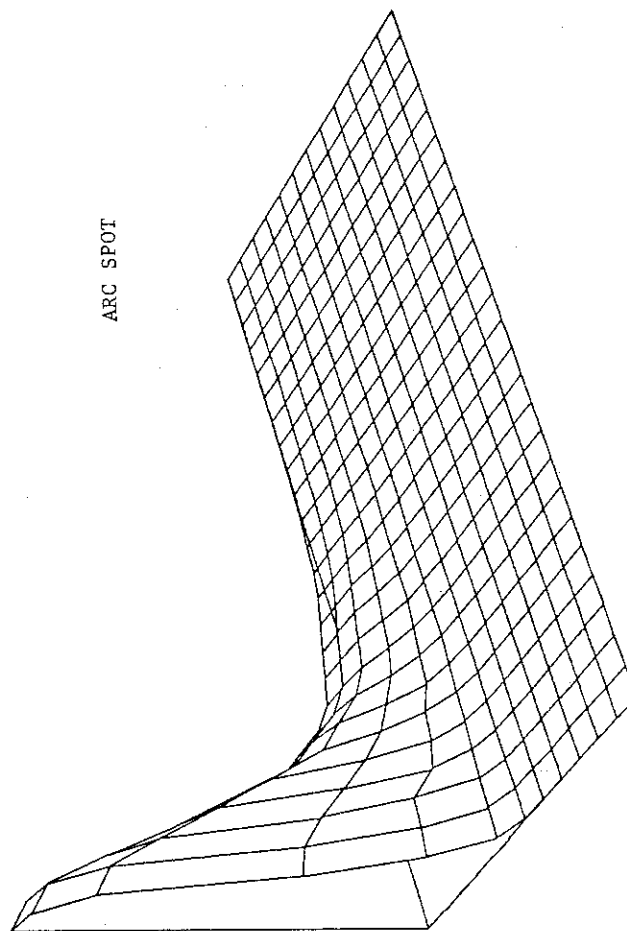
XW   = 100.0
YW   = 200.0
ZW   = 100.0
ALPHA   = -60.0
BETA   = 0.0
GAMMA   = -30.0
L   = 600.0
D   = 200.0

ARC SPOT

ARGUS-V3 ID=BIRD EYE   83-11-08   5 PAGE

Fig. 17   Three dimensional view of temperature rise of the
          heated surface on the WALL3B model.

COPPER 90% H+ BUCKET THERMAL STRESS DUE TO ARC SPOT (SAPW3B) 11/2/83
ELEMENT TYPE NO. 5
   STRESS : INT

CONTOUR VALUES 10**2

1	27.1
2	42.6
3	58.1
4	73.6
5	89.1
6	104.6
7	120.0
8	135.5
9	151.0
10	166.5
11	182.0
12	197.5
13	213.0
14	228.5
15	244.0
16	259.4
17	274.9
18	290.4
19	305.9
20	321.4

(N/cm^2)
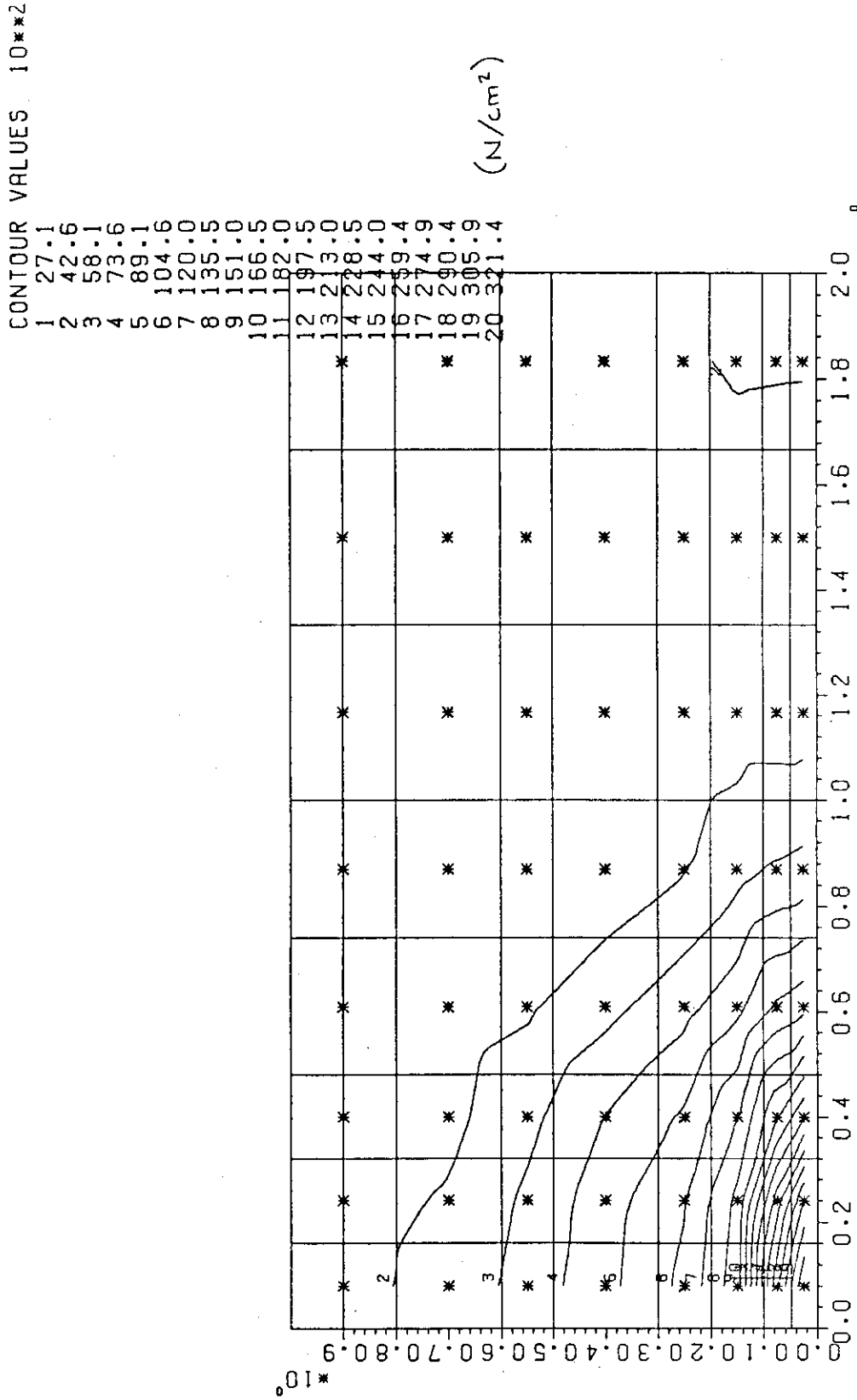
Fig 18 Stress intensity contours of the heated surface of the WALL3B model due to arc spots.
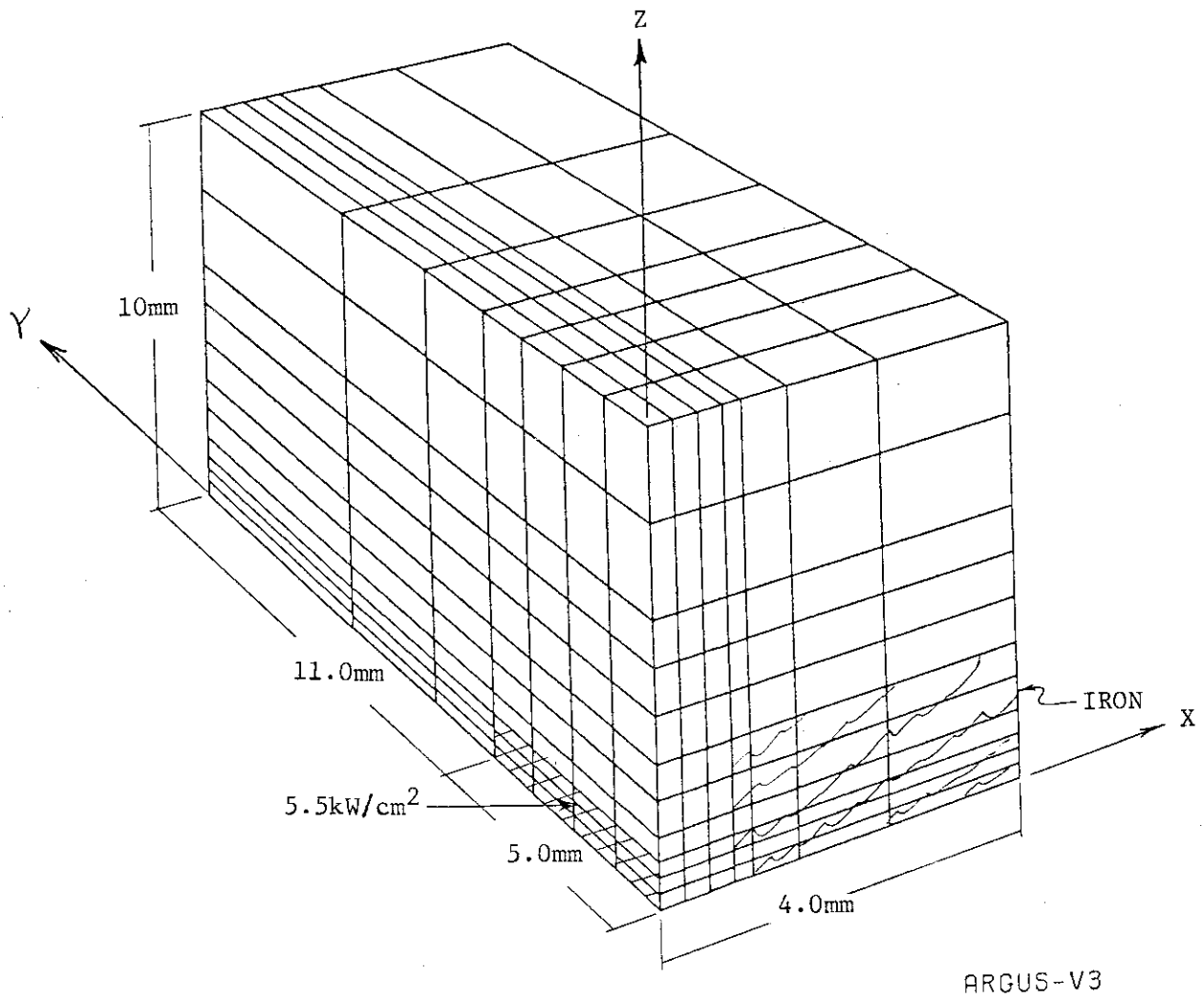
Fig. 19 Three dimensional view of the WALL5 arc spot model mesh.
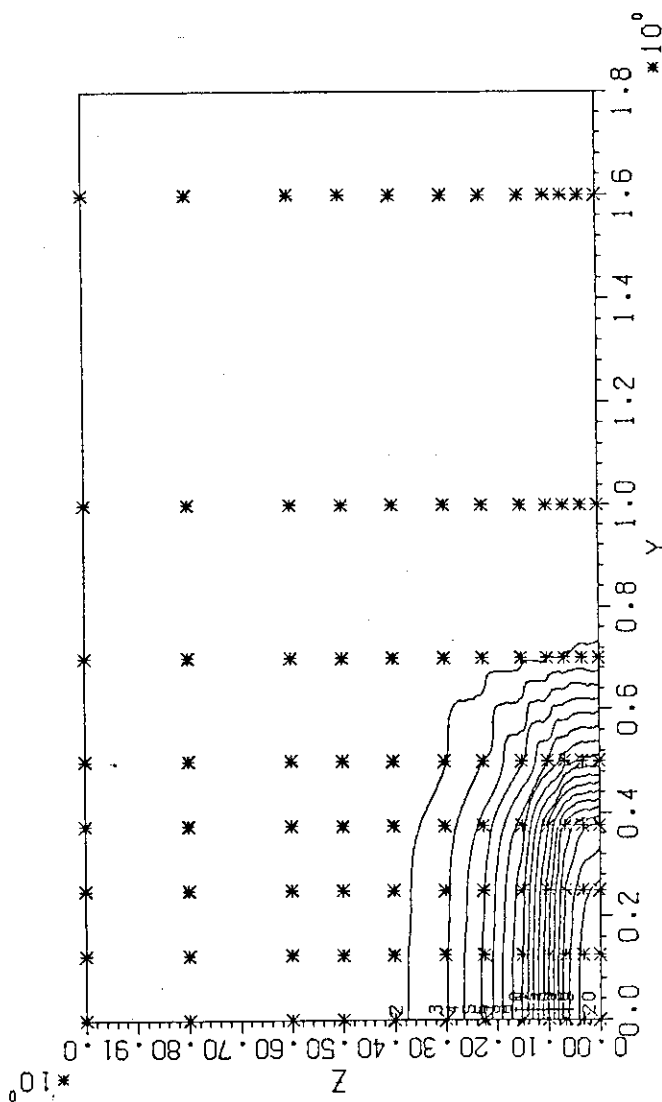
Fig. 20 Temperature contours on the heated surface of the WALL5 model.
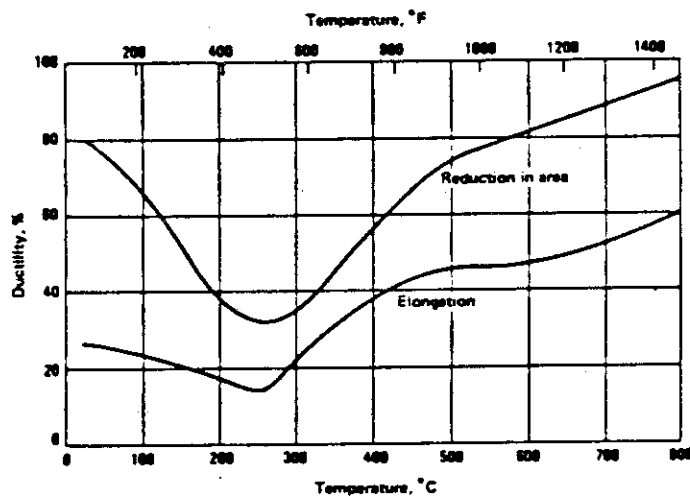
Fig. 21 Ductility of OFHC copper (ASTM C10200) as a function of temperature, from reference 9.
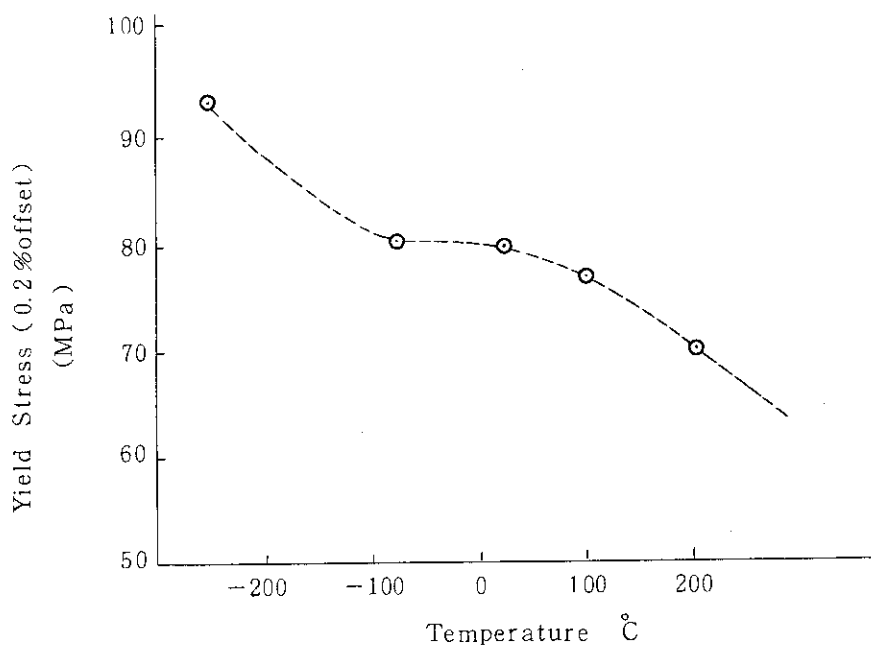

Fig. 22 Yield strength (0.2 % offset) of OFHC copper in annealed condition as a function of temperature. From metals reference book, 5 th ed.
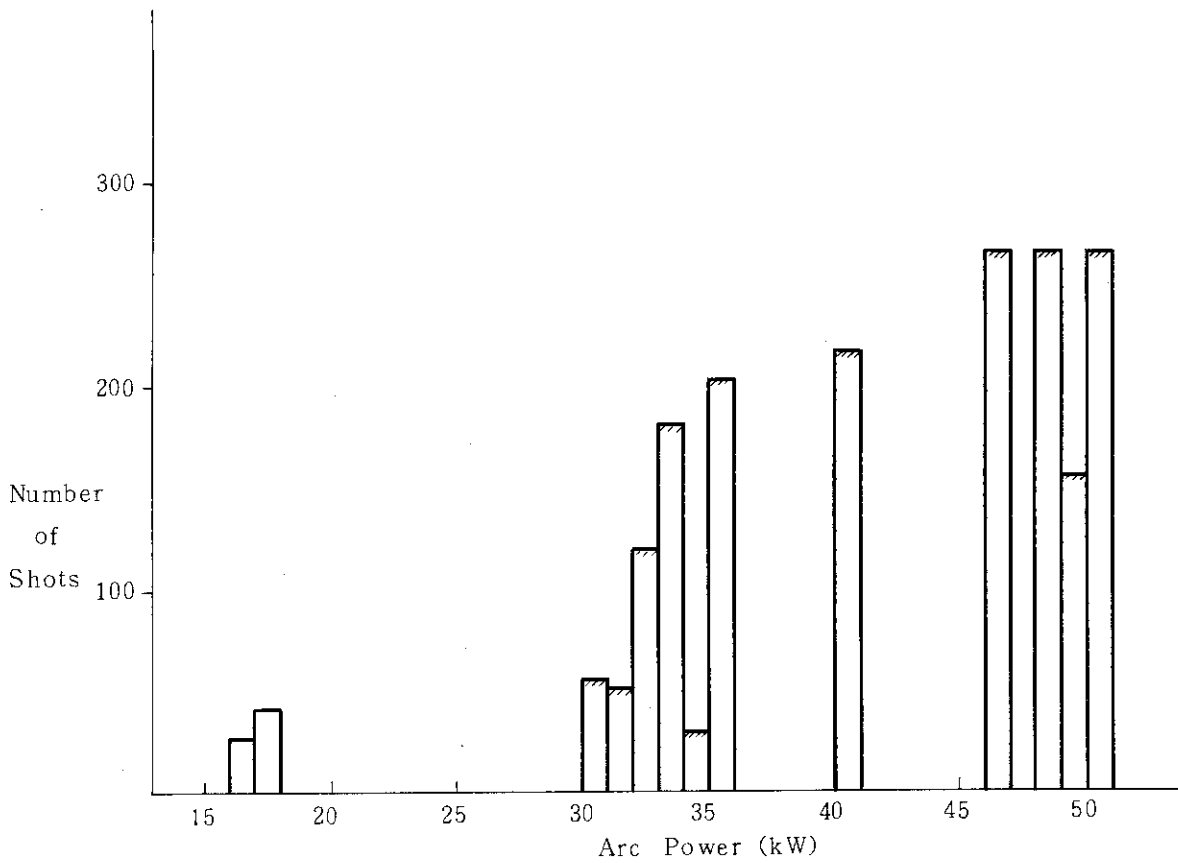
Fig. 23 Summary of "ARC ONLY" tests on the copper large volume bucket ion source
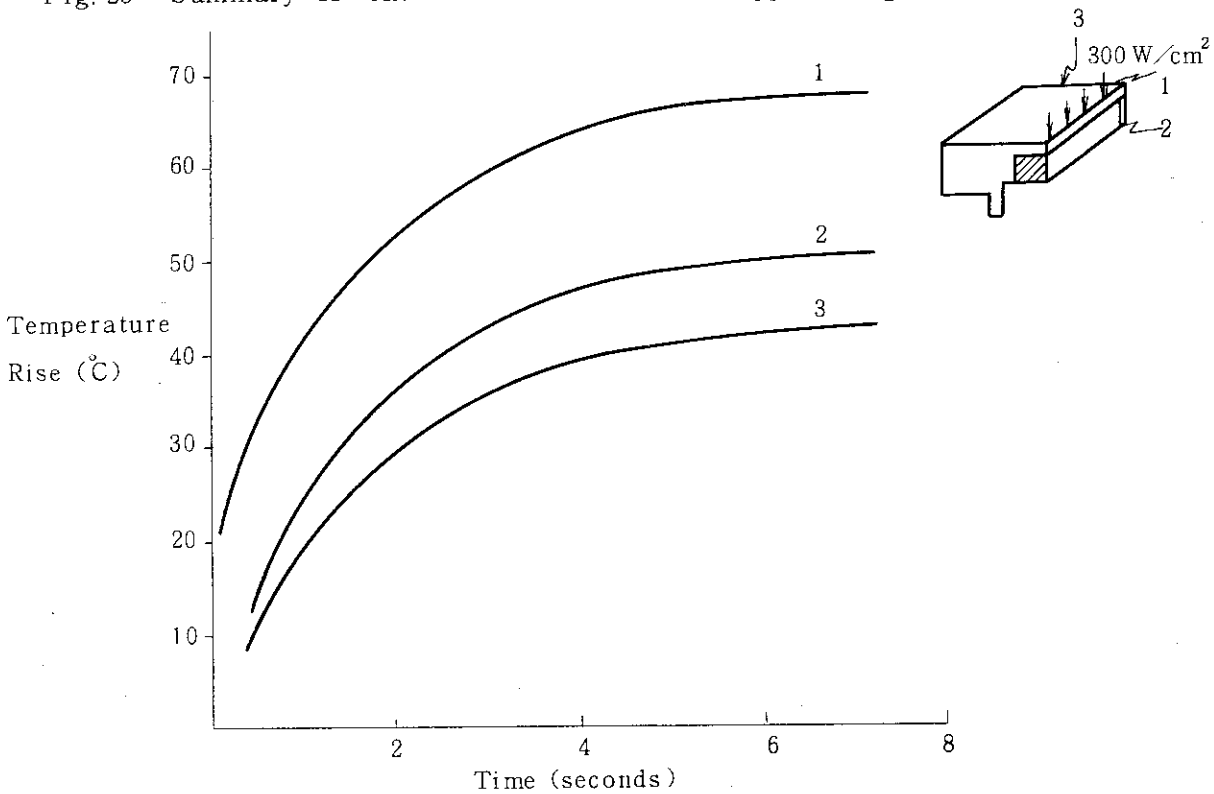

Fig. 24 Temperature as a function of heating time for copper large
volume bucket with 100% iron to Cu. braze. Heat flux is $300W/cm^2$
on cusp line.